Construction and Building Materials 232 (2020) 117205

Contents lists available at ScienceDirect

Construction and Building Materials

journal homepage: www.elsevier.com/locate/conbuildmat

Electrochemical behavior of mild and corrosion resistant concrete reinforcing steels

Muazzam G. Sohail [a], Ramazan Kahraman [b,*], Nasser A. Alnuaimi [c], Bora Gencturk [d], Wael Alnahhal [e], Mina Dawood [f], Abdeldjelil Belarbi [g]

[a] Department of Chemical Engineering, College of Engineering, Qatar University, P.O. Box 2713, Doha, Qatar
[b] Department of Chemical Engineering, College of Engineering, Qatar University, P.O. Box 2713, Doha, Qatar
[c] Center for Advanced Materials, Qatar University, P.O. Box 2713, Doha, Qatar
[d] Sonny Astani Department of Civil and Environmental Engineering, University of Southern California, Los Angeles, CA, USA
[e] Department of Civil and Architectural Engineering, College of Engineering, Qatar University, P.O. Box 2713, Doha, Qatar
[f] Department of Civil and Environmental Engineering, University of Houston, Houston, TX, USA
[g] Department of Civil and Environmental Engineering, University of Houston, Houston, TX, USA

HIGHLIGHTS

- High-chromium steel showed 1.5 times higher *Rp* values than mild steel.
- EIS is the most suitable technique to evaluate the corrosion performance of ECR.
- High-chromium steel showed 48% less macrocell current than mild steel.

ARTICLE INFO

Article history:
Received 26 April 2019
Received in revised form 16 September 2019
Accepted 9 October 2019

Keywords:
Reinforced concrete corrosion
Mild steel
High-chromium steel
Epoxy coated rebar
Infrastructure durability
Electrochemical impedance spectroscopy

ABSTRACT

An experimental study is carried out in this paper to evaluate the corrosion performance of mild steel reinforcing bars (MS), high strength steel reinforcing bars (HS), epoxy-coated steel reinforcing bars (EC), and high-chromium steel reinforcing bars (HC) under harsh environmental conditions. Reinforcing bars (rebar) of 16 mm diameter and 310 mm length were embedded in cylindrical concrete samples of 60 mm diameter and 350 mm length, and subjected to a Southern Exposure test for sixteen months. The open circuit potential (OCP) was monitored during the exposure period until corrosion initiation. The linear polarization resistance (LPR), electrochemical impedance spectroscopy (EIS), and Tafel plot techniques were employed to assess the corrosion rates on the rebar surfaces. The macrocell corrosion current was monitored by connecting the corroding rebar with an external stainless steel bar of the same size. The polarization resistance of the HC was found to be 1.5 times higher than that of the MS. The EIS technique showed that EC, even with damaged epoxy coating, has the highest resistance to chloride attack. The macrocell current of HC rebar was 48% less than that of MS during the active corrosion state. The LPR, EIS and Tafel plots analysis provided the current densities, which were close to each other; indicating the validity of these techniques to study the problem at hand. The corrosion rates from electrochemical methods were compared against the ones calculated by gravimetric methods. The quantitative results from this research may be used in service life prediction of concrete structures with different types of rebar. Extensive analysis of the results indicates that the corrosion resistance of the evaluated steels was in the following decreasing order: EC, HC, MS, and HS.

1. Introduction

Corrosion of reinforcing steel bars (rebar) in concrete is a major cause of civil infrastructure degradation around the world. The repair cost of the damaged infrastructure due to the corrosion is reported to be up to 3% of the gross domestic product (GDP) of the developed countries [1,2], and it is up to 5% in the Middle East where harsh climates such as high temperature, humidity and airborne chlorides are encountered [3]. To overcome corrosion related degradation, it is recommended to improve the quality of concrete and use more concrete cover to prolong the initiation phase.

* Corresponding author.
E-mail address: ramazank@qu.edu.qa (R. Kahraman).

https://doi.org/10.1016/j.conbuildmat.2019.117205
0950-0618/

Employing corrosion resistant rebar such as epoxy coated steel rebar (EC), high chromium steel rebar (HC), and stainless steel rebar (SS) with higher chloride threshold could delay the initiation and slow down the progression of corrosion. The epoxy coating provides a physical barrier against the chloride ions and retards the initiation of corrosion. Moreover, it has a higher resistance to electric charge; hence, no macro-cells are formed unless defects are generated within the rebar [4,5]. The high chromium steel standardized under ASTM A1035/A1035M-16b has a chromium content up to 9–11% and a carbon content of 0.1% [6]. The microstructure consists of untransformed nano-sheets of austenite between laths of dislocated martensite and the formation of carbides is avoided. This results in a steel alloy with improved corrosion resistance and high strength [7].

Several field and laboratory studies carried out to evaluate the corrosion performance of EC in concrete yielded mixed results. However, it is widely accepted that the durability of reinforced concrete (RC) structures improves when EC is used [4,8,9,64]. Pyc performed a field study on 18 concrete bridges after 7–20 years of service life [8]. It was observed that the epoxy looses its adhesion with the steel surface over time due to the moisture ingress. However, Keßler et al. suggested otherwise after evaluating the parapet of a 24 years old EC-reinforced-concrete bridge in Switzerland [4]. After 24 years of service life in a region with XD3 exposure conditions according to EN 206-1 [10] (i.e., an average 10 days rain per month), it was observed that the epoxy coating was in good condition with a shining green color, and no damage or disbondment was noticed due to moisture. Erdoğdu et al. tested EC in comparison with mild steel rebar (MS) under seawater and a synthetic solution with 3% $NaCl^-$ [11]. EC was used in three conditions, as-received, and with 1% and 2% controlled damage. The damage was generated by removing the coating in 6 × 6 mm squares using a hand grinder. After two years of exposure under chloride environment, no signs of corrosion was observed on the undamaged EC. The EC with 1% and 2% damage had negligible corrosion in the damaged area [12].

In case of HC, the manufacturers suggest that its corrosion resistance is similar to that of SS. However, several studies carried out to evaluate the corrosion resistance of HC in comparison to low carbon MS and SS, have found that its corrosion resistance is higher than that of MS; however, lower than that of SS [13–16]. Nachiappan and Cho observed that the corrosion rates of HC are sensitive to the chloride concentration [15]. It was observed that when bare rebar of HC and MS are placed in 0.1% chloride solution, the corrosion rate of MS is 12 times higher than that of HC. However, when chloride contents are increased to 3%, only 3-times higher corrosion rate was observed for MS compared to HC. Two times higher corrosion currents are observed on MS compared to HC embedded in concrete after 132 days of exposure to a chloride solution. Mohamed et al. reported that the lifespan of RC structures could be enhanced by 10–30 years by employing HC than MS [21]. This conclusion was based on the assumption that chloride attack at the surface of concrete is 0.25 M and the concrete diffusion coefficient is 9.4×10^{-12} m^2/s. Fahim et al. evaluated the performance of MS, HC, 316 LN SS, 304 SS, and XM 28 SS in simulated concrete pore solutions and un-cracked and cracked concrete medium [22]. It was observed that the alloy composition of all steel rebar plays a significant role in the chloride threshold values that initiate corrosion, the passive layer composition and the corrosion rates. In the experiments performed on mortar samples, the HC showed a corrosion rate of 50–60% of that of MS. However, SS with higher percentage of chromium, nickle and nitrogen, out performed HC in terms of corrosion resistance in all mediums.

The corrosion performance of EC is normally evaluated by visual inspection, half-cell potential (HCP) and linear polarization resistance (LPR) techniques [8,9,11]. The LPR applies a direct current, which may not be able to pass through the epoxy and hence might lead to erroneous results. Furthermore, the models to predict the service life of RC structures are heavily dependent on the corrosion rates of reinforcement after the corrosion initiation [18–21]. Studies are carried out to evaluate the corrosion of MS, HC and EC in either simulated concrete pore solutions or in concrete block/slab/prism samples. The block samples do not allow for uniform polarization of the rebar during the electrochemical testing.

In this study, a comparative corrosion performance of four types of concrete reinforcements, MS, HC (9% Cr content), EC, and high-strength steel rebar (HS) that is locally manufactured in Qatar, is presented. Although, higher strengths were achieved by changing the chemical composition of the steel (higher carbon and chromium contents), corrosion resistance of these steel alloys needs to be investigated. A sample geometry is selected such that the environmental corrosion and the error in estimating the polarized surface area during electrochemical tests are minimized. The parameters used for numerical modeling of corrosion in RC are established for MS, HS, and HC rebar. The electrochemical impedance spectroscopy (EIS), which is proven to be the most suitable approach to study the corrosion performance of epoxy coating and the corrosion of underlying steel, was employed. The quantitative results from this research may be used for service life prediction of concrete structures. This comparative study also provides engineers with data to select the type of rebar according to the environmental conditions that RC structures will have to withstand during their lifespan. A comparison of three electrochemical techniques for corrosion rate estimation is also provided.

2. Experimental program

2.1. Materials

2.1.1. Steel rebar

The studied MS, HS, HC, and EC conformed to BS 4449:2005 [63], Grade 80 of ASTM A615/A615M-16 [19], ASTM A1035/A1035M-16b 2016 [6], and ASTM A775/A775M-17 [23], respectively. The chemical composition of the rebar, as provided by the manufacturers, are given in Table 1. The yield and tensile strengths are shown in Table 2. Initial weights of steel rebar were measured using a balance with 0.01 g sensitivity. The EC were patched with epoxy at the ends after cutting them at required lengths.

2.1.2. Concrete mixture proportions

The mixture proportions of the concrete used to cast the samples are given in Table 3. Type I Portland cement, gabbro aggregates with a maximum size of 10 mm, washed sand with 0-4.75 mm size and a polycarboxylate ether (PCE) based Epsilon PC 485 superplasticizer were used as ingredients. The particle size distribution of coarse gabbro aggregates and washed sand are presented in Fig. 1. A maximum aggregate size of 10 mm was necessary due to the small sample dimensions. The concrete had a flow spread of 535 mm with T_{50} of 7.8 s according to ASTM C1611/C1611M-14 [24]. The interior surface of the cardboard molds was waxed to prevent water absorption from the concrete paste. The concrete compressive strength was obtained as 38 MPa from testing of six cylindrical samples of 100 × 200 mm dimensions according to ASTM C39/C39M-15a [25] at 28 days.

2.2. Sample geometry

Twenty-four concrete cylinders 60 mm in diameter and 350 mm long were cast. One MS, HS, EC or HC having 16 mm diameter and 310 mm length, was embedded at the center of concrete cylinders. A concrete cover of 22.5 mm circumferentially and

Table 1
Chemical composition of steel rebar as provided by manufacturers.

Steel Type	Chemical Composition (%)												
	C	Si	Mn	P	S	V	Nb	Cu	Ni	Cr	Mo	N	Ce
MS	0.200	0.140	0.660	0.011	0.014	–	–	0.025	0.021	0.013	–	0.006	0.320
HS	0.300	0.240	1.160	0.014	0.017	0.015	0.028	0.016	0.027	0.029	–	–	0.510
EC	0.230	0.130	0.720	0.007	0.010	–	–	0.019	0.018	0.014	–	0.005	0.350
HC	0.100	0.410	0.570	0.011	0.009	0.270	0.019	0.160	0.100	9.540	0.020	0.019	1.150

Table 2
Mechanical properties of steel rebar as provided by manufacturers.

Steel Type	Strength	
	Yield Strength MPa	Tensile Strength MPa
MS	561	664
HS	637	735
EC	597	678
HC	937	1158

Table 3
Concrete mixture proportions.

Constituents	Units	Quantity
Cement (CEM I)	kg/m^3	410
Washed sand, 0/4.75 mm	kg/m^3	962
Coarse aggregate, 0/10 mm	kg/m^3	951
Water	kg/m^3	159
Water-cement ratio	–	0.45
Superplasticizer	kg/m^3	5.2

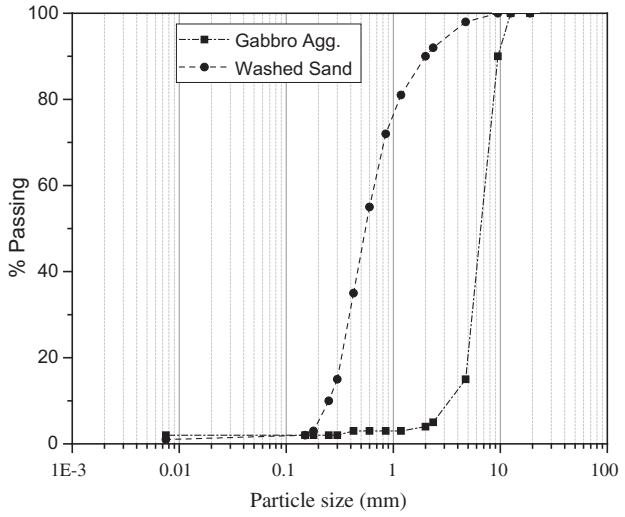

Fig. 1. Particle size distribution of coarse aggregates (agg.) and washed sand.

25 mm at the top and bottom was provided. Six samples for each type of steel were prepared to ensure that the variability in the material properties and testing procedures is properly captured. Samples were designated based on the type of steel, i.e., MS, HS, HC, or EC followed by a number from 1 to 6, e.g., first mild steel sample is designated as MS-1, and so on. A copper wire was connected to rebar to establish the connection for electrochemical measurements. In the case of EC, a 2 mm wide portion of the epoxy was removed circumferentially to establish electrical connection to the steel. Silicon paste was applied at connection to prevent humidity and chloride ingress. After casting, the wire-concrete interface was covered with silicon paste to prevent the ingress of chloride containing water. The cylindrical geometry enables uniform polarization of rebar and eliminates the errors in the estimation of polarized-steel-area during electrochemical tests. The steel rebar was completely embedded in concrete to avoid environmental corrosion.

2.3. Accelerated aging conditions

The Southern Exposure test conditions, i.e., cycles of four days of wetting by ponding under 15% $NaCl^-$ solution followed by three days of drying in the open air, were applied for 16 months. Samples were immersed in a salt solution horizontally as shown in Fig. 2. They were submerged at least 2 cm below the water surface during the ponding period. The water containing chlorides penetrates through concrete pores during the wetting period and the evaporation during drying leaves chloride ions on the concrete surface. This creates a chloride ion concentration gradient, enabling the diffusion process to transport these ions to the steel-concrete interface. The open circuit potential (OCP) (or half-cell potential, HCP) was measured at regular intervals to determine the corrosion initiation times of each type of rebar.

3. Testing methods

3.1. Concrete resistivity and sorptivity

Concrete resistivity was measured on cylindrical samples of 100 × 200 mm at 28 days of curing according to AASHTO TP 95 [26]. Measurements were performed on three cylinders to obtain an average as recommended by the Standard. The samples were in quasi-saturated state at the time of measurements. Table 4 presents the corrosion risk associated with the concrete resistivity values. At a resistivity higher than 20,000 Ohm-cm, corrosion risk is negligible, while at resistivity less than 5000 Ohm-cm, very high corrosion risk exists [26,27].

Fig. 2. The samples immersed in 15% $NaCl^-$ solution during wetting cycle of Southern Exposure test.

Table 4
Corrosion risk as a function of concrete resistivity [26].

Resistivity (Ohm-cm)	Corrosion Risk
>20,000	Negligible
10,000–20,000	Low
5000–10,000	High
<5000	Very high

The sorptivity is a measure of the moisture transport into unsaturated concrete, a good quality concrete shows low sorptivity. The sorptivity of three concrete disk samples of 100 × 50 mm was measured according to ASTM C1585-13 [28] after 28 days of curing.

3.2. Chloride content

The chloride contents were measured at three locations, at outer concrete surface, at middle of the sample, and at the steel-concrete interface (i.e., at a depth of 22.5 mm), after 16 months of exposure on four concrete samples according to BS 1881: Part-124 [29]. One concrete sample from each category was broken after all the electrochemical tests. This test yields the results in chloride content by percentage mass of concrete. However, as it is commonly adopted in literature, to present chloride threshold values for corrosion initiation by percentage mass of cement [30,31], chloride profiles were presented in both percentage mass of concrete and cement.

3.3. Electrochemical tests

3.3.1. Half-cell potential

The HCP of steel rebar was monitored at regular intervals against the saturated calomel electrode (SCE) as a reference. HCP values were recorded after wetting cycles with the samples placed in water in quasi-saturated state. Readings were noted once the HCP becomes stable. ASTM C876-09 [42] relates the HCP to the probability of corrosion of rebar in concrete. Table 5 shows the ranges associated with low to severe risk of corrosion.

Table 5
Half-cell potential values for corrosion conditions [32].

HCP Values		Corrosion Conditions
mV vs. SCE	mV vs. CSE	
Less than-426	Less than-500	Severe corrosion
Less than-276	Less than-350	High (higher than 90% risk of corrosion)
−126 to −275	−200 to −350	Intermediate corrosion risk
Higher than −125	Higher than −200	Low (10% risk of corrosion)

3.3.2. Linear polarization resistance

Once the corrosion initiation was determined based on the HCP values, the corrosion rates were measured by LPR, EIS and Tafel plots. These techniques were applied using the three-electrode setup shown in Fig. 3. A working electrode (WE), that is the steel rebar inside the cylindrical concrete samples, a counter electrode (CE), that is a non-corroding titanium mesh, and a reference electrode (RE), that is the SCE were used. During testing, the samples were partially immersed into the water, this was to keep the samples quasi-saturated and to ensure the availability of oxygen at the steel-concrete interface.

To obtain the LPR curves in this study, a ±20 mV polarization (OCP − 20 mV to OCP + 20 mV) with a scan rate of 0.167 mV/s was applied on the steel rebar and the current response was recorded. Gamry® 600 potentiostat was used for these experiments.

3.3.3. Electrochemical impedance spectroscopy (EIS)

The EIS is a powerful technique to analyze the electrode (rebar) charge transfer resistance, R_{ct}, double layer capacitance, C_{dl}, and the electrolytic (concrete) resistance and capacitance, R_c. A small (5–25 mV) sinusoidal voltage, $V(t) = V_0\sin(\omega t)$, at a selected range of frequency, $f = \frac{\omega}{2\pi}$, is applied to perturb the corroding rebar. The steady state current response, $I_t = I_0\sin(\omega t + \theta)$, is measured, which has a phase difference of θ from the applied voltage. The impedance, $Z = \frac{\Delta E}{\Delta I}$, is then measured using Ohm's law [33–35]. In this study, the EIS spectra is presented in the form of a Nyquist plot, which shows the impedance in the complex plane of Cartesian coordinates, i.e., $Z = Z' + jZ''$, where Z' and jZ'' are the real and imaginary parts and drawn on the abscissa and ordinate of the plot, respectively.

Fig. 4a schematically presents the different physical interfaces encountered in the steel reinforced concrete during the impedance scan. From left to right are the bulk concrete resistance, the interfacial layer between concrete and steel rebar (rust products with lime precipitation on the steel surface) and the double layer-electrode interface. Depending upon the geometry of corrosion system in concrete, the schematic of typical Nyquist plot for the EIS spectra in RC is shown in Fig. 4b [35]. Three capacitive semicircles appear at different frequency ranges, at higher frequencies

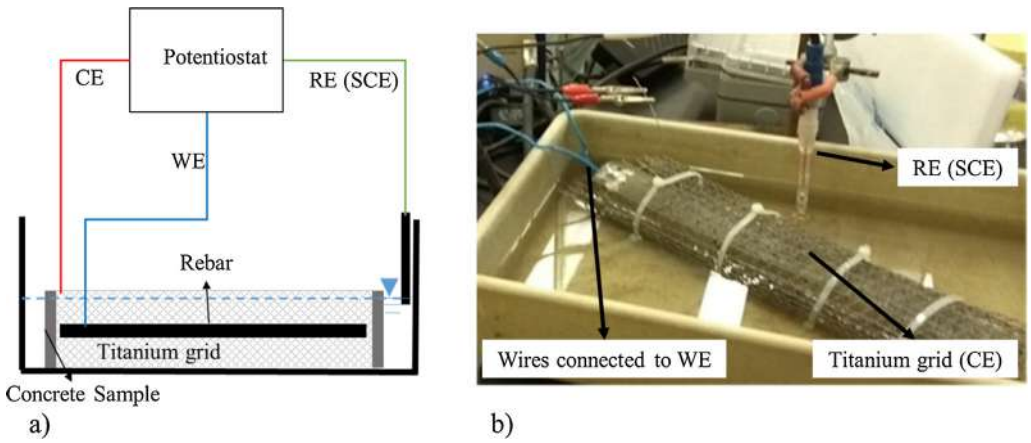

Fig. 3. Three electrode set up: a) schematic, b) actual experimental set up.

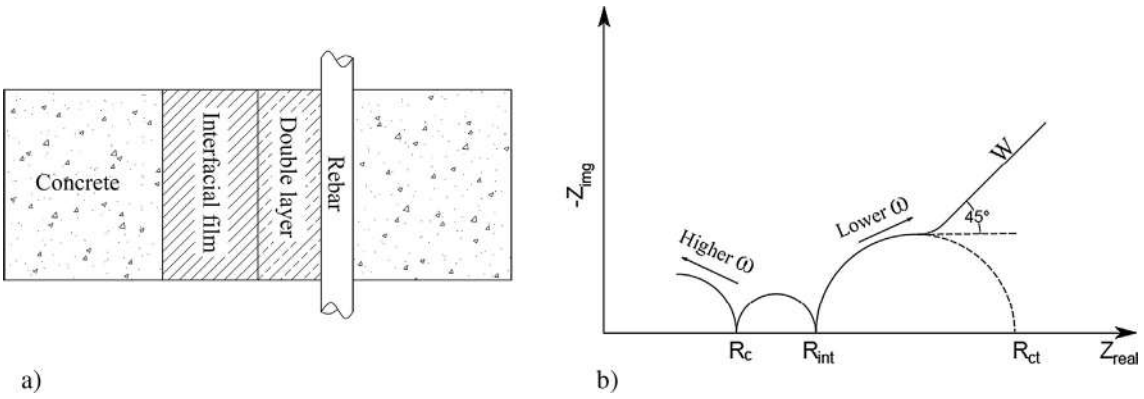

Fig. 4. a) Schematic of physical interfaces, b) Nyquist plot of corrosion system in steel RC.

bulk concrete characteristics are obtained, while the lower frequencies provide the information on the rebar conditions. In some cases, the diffusion of ions through the oxide layer coupled with a Faradaic reaction is observed at lower frequencies on the steel surface. Nyquist plots are compared to an equivalent circuit model to extract the parameters, such as the R_c, R_{ct}, C_{dl}. In case of EC, the epoxy coating resistance, R_{EC}, and capacitance, C_p are also obtained [12,64]. In this study, to obtain the EIS spectra, a voltage of 10 mV was applied at a frequency range of 0.001 Hz–8 MHz to the steel rebar using a Zehner® Zennium Pro potentiostat. The ZMan™ 2.4 software was used to fit the experimental data against automatically selected equivalent circuit models. Equivalent circuit models and extracted parameters are presented in Results and Discussion section.

3.3.4. Tafel plot

The Tafel plot is an established technique to calculate the corrosion current, I_{corr}, on a metal surface. Corrosion reaction rate is quantified by log I vs E curves, also known as the polarization curves [36]. A polarization of ±200 mV from OCP (OCP to −200 mV to OCP +200 mV) was applied to steel rebar with a scan rate of 0.167 mV/s and the logarithmic response of the current, I, was recorded. A Gamry® 600 potentiostat was used to obtain Tafel polarization curves. The extrapolation of these curves was performed to obtain the corrosion parameters such as corrosion potential, E_{corr} , corrosion current, I_{corr}, anodic Tafel slope constant β_a and cathodic Tafel slope constants β_c. From I_{corr}, the corrosion current density per unit area, i_{corr} in $\mu A \cdot cm^{-2}$ is calculated using $\Delta I/S$, where S is the polarized steel surface area. The Tafel polarization is a destructive technique and was performed after LPR and EIS scans.

3.3.5. Macrocell current

Macrocell corrosion current was generated by connecting the embedded steel rebar to an external equal sized SS through a zero resistance ammeter (ZRA), Gamry® 600. The equal sized cathode bar provides a cathode/anode ratio of 1. The SS and the concrete cylindrical sample were placed inside the water. Electron flows from the embedded rebar to the SS, simulating the connection between the active steel and passive steel in RC during galvanic (macrocell) corrosion. Measurements were carried out until a steady-state macrocell current is reached.

4. Results and discussion

4.1. Concrete resistivity and sorptivity

The concrete resistivity was measured as 25.041 kΩ · cm, which indicates that the corrosion-risk associated with such a high resistivity is negligible according to AASHTO TP 95 (2011) [27,37]. The initial sorptivity of concrete was found as 0.0043×10^4 mm. $s^{-1/2}$, which is in the range of values for normal concrete reported in the literature [39,39].

4.2. Chloride profiles

Fig. 5 shows the chloride profile at different depths after 16 months of exposure. The average, minimum and maximum chloride values over four samples are presented. Although the tested concrete was the same for all the samples, a slight variation in the chloride contents is observed. Since slices of 7 mm were cut from the broken concrete samples, this variation could be due to the irregularities in the cutting. Additionally, the extracted powder sample could be from opposite end of 7 mm slice. The chloride contents reached around 1% of concrete mass and 5.5% of cement mass at the outer surface of the samples, as presented in Fig. 5. At the steel-concrete interface, the chloride concentration reached between 0.47% and 0.74% of the concrete mass and 2.5% to 3.7% of the cement mass. These values are at least three to four times higher than the threshold values for corrosion initiation of MS in concrete [30].

4.3. Half-cell potentials

The HCP of MS, HS and HC are as shown in Fig. 6. HCP decreased during the first few weeks, before becoming stable for a period of time, then it dropped to more electronegative values. At the time of LPR, EIS, and Tafel plot tests, the HCP of six samples varied from −595 mV/SCE to −703 mV/SCE for MS, from −463 mV/SCE to −573 mV/SCE for HC steel, and from −649 mV/SCE to −762 mV/SCE for HS. According to ASTM C876-09 [40], the probability of corrosion initiation on the steel surface is above 90% once the HCP drops below −426 mV/SCE. The corrosion susceptibility for uncoated rebar based on HCP was in the following order from highest to lowest: HS, MS and HC. The HCP of EC was also recorded; however, the measured values were not representative, as they were very electronegative, which is attributed to the corrosion at the location of the electrical connection and the broken patched ends of the rebar. It is believed that the water and chloride ions penetrated through the silicone gel applied at the connections. For these reasons, the HCP for EC are not presented in this study.

Similar HCP ranges were reported for MS and HC at an active corrosion state by Fahim et al. [13] and in chloride contaminated concrete and by Mohamed et al. [17] in a $NaCl^-$ solution. The average drop in HCP values from a passive to an active corrosion state was lowest for HC among the three types of uncoated steel rebar. The smaller shift of HCP from passive to active corrosion state will generate a lower electromotive force during macrocell formation

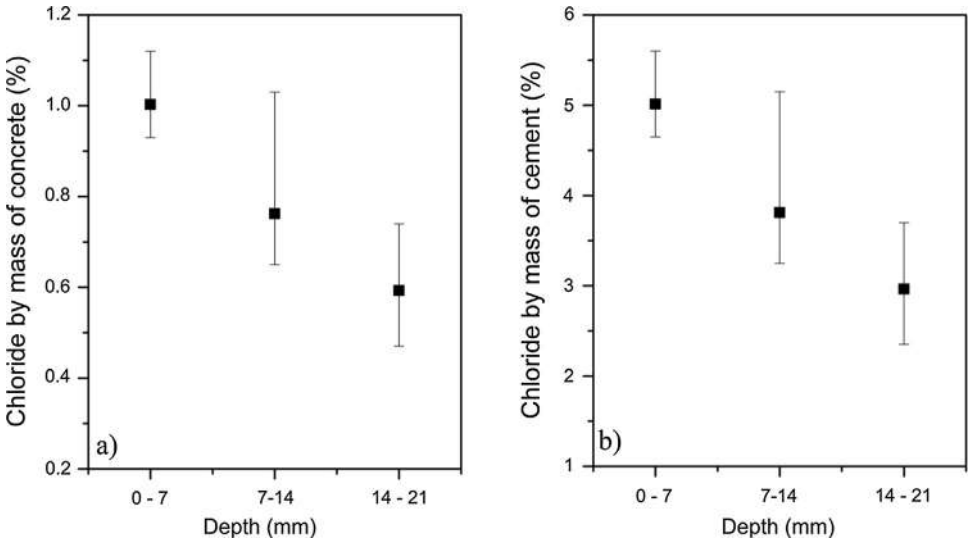

Fig. 5. Chloride profile along the depth of concrete samples after 16 months of exposure, a) % mass of concrete, b) % mass of cement.

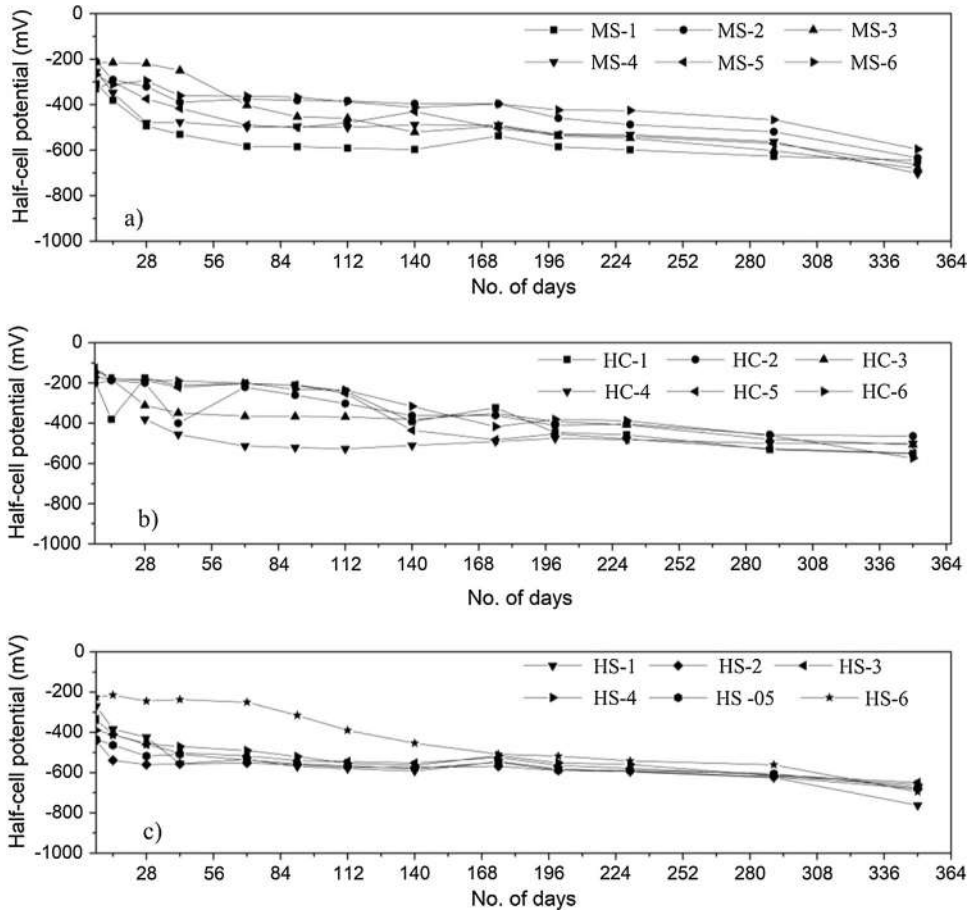

Fig. 6. Half-cell potential monitoring: a) MS, b) HC and c) HS.

in the reinforcement mesh; hence, less macrocell corrosion current.

4.4. Linear polarization resistance

Fig. 7 presents the selected LPR curves for MS, HS and HC. HS showed a quasi-linear behavior in the entire polarization range; however, a nonlinear response started near −20 mV polarization for MS and HC as shown in Fig. 7a and b, respectively. Only the linear portion of the LPR curves was analyzed to calculate R_p. Since in LPR technique a 5 mV to 20 mV of polarization is recommended [41], the linear portion in these ranges could be analyzed to obtain the polarization resistance.

The nonlinear portion near −20 mV is attributed to the experimental set-up inside the water. Since the scan starts from −20 mV from OCP, there could be some astray current between titanium

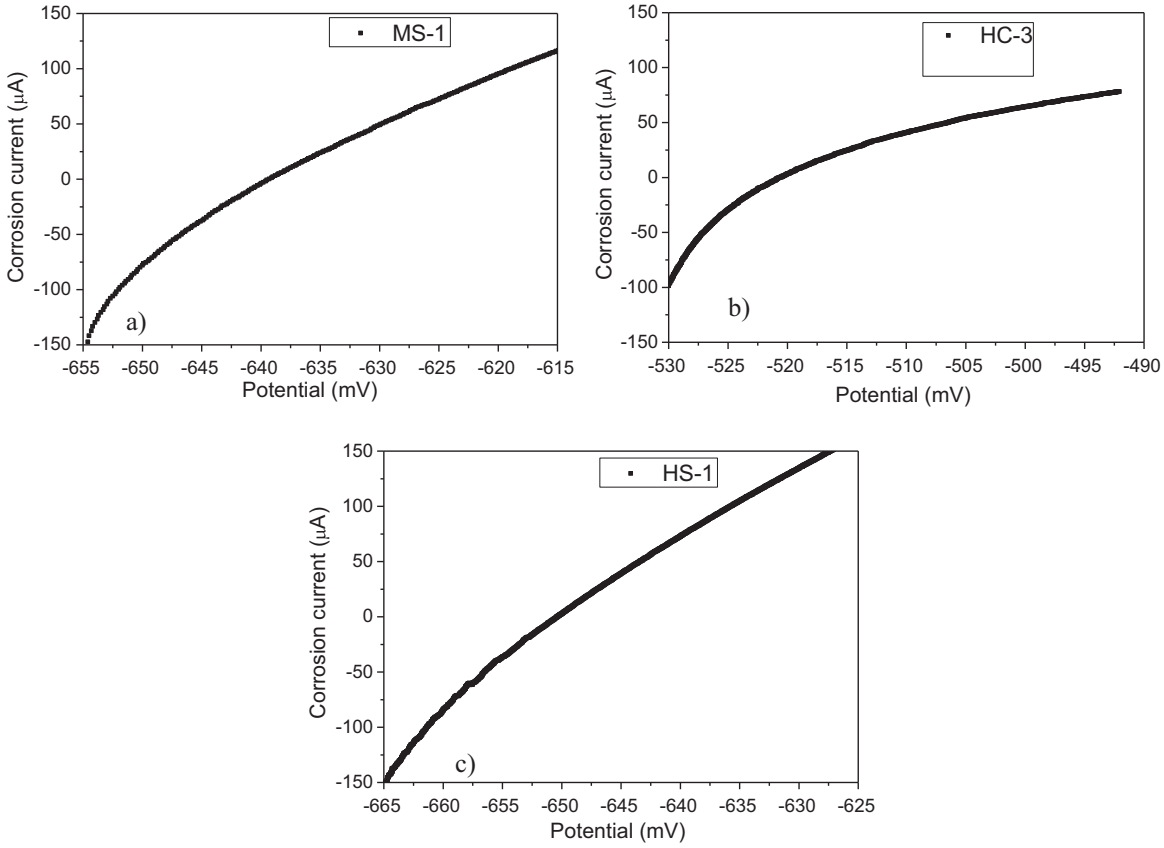

Fig. 7. Linear polarization curves for a) MS, b) HC and c) HS.

mesh and water around this voltage. The average R_p values over six samples were 57 kΩ.cm^2, 39 kΩ.cm^2 and 14 kΩ.cm^2 for HC, MS and HS, respectively. R_p values lower than 230 kΩ.cm^2 indicate an active corrosion state [42]. The measured values were much less than 230 kΩ.cm^2, especially for HS. This shows a higher corrosion activity on the HS surface. In the active corrosion state, HC showed 1.5 times higher R_p values than MS and at least four times higher than HS, and hence indicating a higher resistance to corrosion based on the corrosion rate. The average value and the standard deviation of R_p based on the measurements of six samples are presented in Section 4.5 in comparison with the values obtained from EIS.

4.5. Electrochemical impedance spectroscopy

Fig. 8 shows the Nyquist plots of the studied rebar during active corrosion state inside the chloride contaminated concrete. The MS, HC, and HS showed a similar behavior. The EC had a slightly different Nyquist plot shape than the uncoated rebar at higher frequency ranges, i.e., towards the right of the Nyquist plot. The noise in EC curves is due to the corrosion of connections. The frequency ranges of each capacitive arc are indicated in Fig. 8. The space of the electrochemical impedance spectra was found to be in acceptable range since corroding rebar offer less polarization resistance, chloride contaminated concrete also offers less resistance to electrical charge. Therefore, the Nyquist plot gets closer to zero than for passive rebar and dry and chloride free concrete. Similar space spectra were obtained by several other researchers [33,43]. Vedalakshmi and Palaniswamy observed similar ranges of Nyquist plot in the active corrosion state of rebar in concrete after 1135 days of conditioning in a chloride solution [42]. Considering the physical impedance phenomenon in RC, two proposed equivalent circuit models, shown in Fig. 9, were fitted against the experimental results. The resistive, **R**, and reactive, **C**, elements appear in series or parallel in the circuit to simulate the physical impedance of the RC system. The total resistance constitutes the bulk resistance of concrete, the resistance of the rust product having lime ($Ca(OH)_2$) precipitation, the resistance of the steel-concrete interface, and the Warburg diffusion. Several researchers [33,35,44,45] have used similar circuit models with minor differences. Since concrete is a heterogeneous material and many intermixed interfacial regions contribute to the impedance spectra, the capacitive arcs overlap in the Nyquist plot. Further, the concrete and the steel-concrete interface are not pure capacitors. That is why these capacitive arcs, instead of being a perfect semicircle formed above the real axis (as shown in Fig. 4b), they are depressed with their centers below the real axis. To accurately model an equivalent circuit, these imperfect interfaces and electrode-surface-roughness necessitate a constant phase element (CPE), Q_i, in place of a pure capacitor (see Fig. 9). The CPE helps fit the circuit to the experimental spectra. From the CPE, the capacitance of different elements is obtained according to

$$C = Q^{\frac{1}{n}} R^{\frac{1-n}{n}} \quad (1)$$

where n is an index, varying from zero to one, which measures the imperfection of the element. For a pure capacitor, n is equal to one while for a pure resistor it is equal to zero.

The model in Fig. 9a shows that R_{ct} and CPE(Q_3) are in series with R_2, which is the resistance offered by the corrosion product having lime precipitation. At the steel surface, the capacitance of this layer, (Q_2), is in-parallel with the electrode reaction, R_{ct}, Q_{dl}. Fig. 9b presents the circuit with the impedance of rust layer with concrete products, R_2, Q_2, which are in series with the electrode reactions, R_{ct}, Q_{dl}.

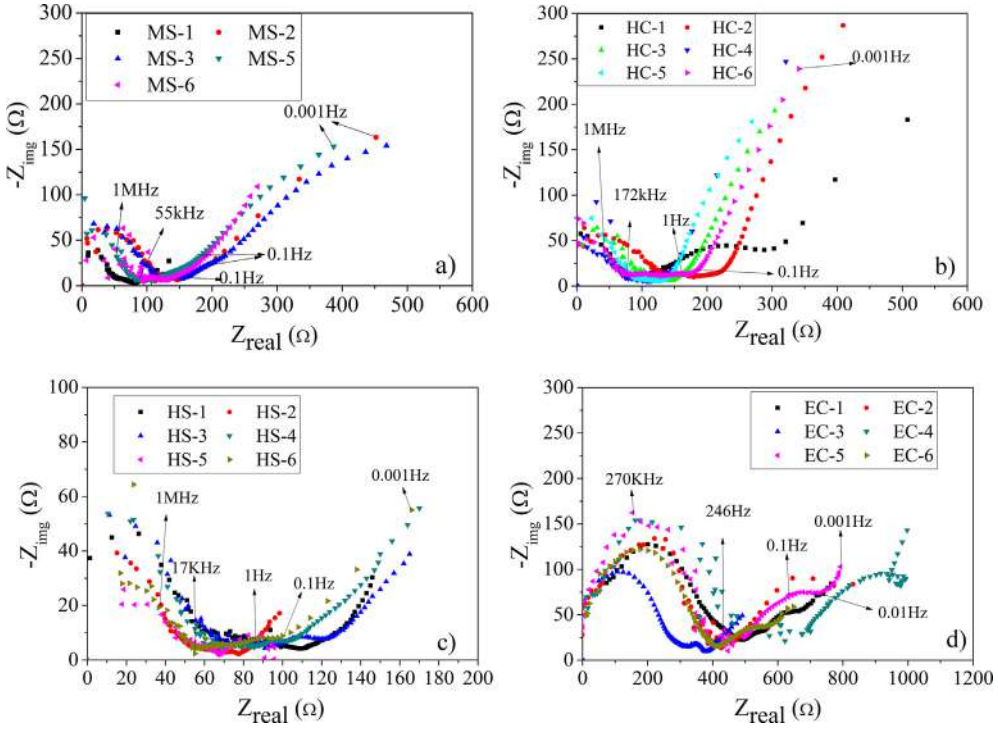

Fig. 8. Typical Nyquest plots with frequency cut offs for overlapping semi-circles. a) MS, b) HC, c) HS, d) EC. Frequency ranges for different capacitive arcs are shown for MS-5, HC-6, HS-6, and EC-5.

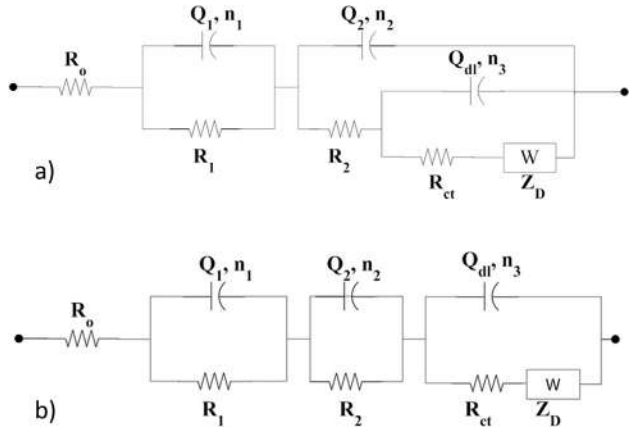

Fig. 9. Equivalent circuit models for the EIS spectra in concrete reinforced with steel rebar.

The arcs in the low-frequency range from 0.1 Hz to 1 Hz on the right side of the Nyquist plot provide R_{ct} and C_{dl}. At further low frequency ranges from 0.001 Hz to 0.1 Hz, W was observed in all samples. The upward rise of the curve at approximately 45°, as shown in Fig. 8, is an indication of the semi-infinite diffusion of species such as oxygen, iron, hydroxyl, and chloride ions through the oxide layer and towards the electrode, coupled with charge transfer reactions. The Warburg impedance is calculated by

$$Z_D = \frac{1}{W\sqrt{\omega}} \quad (2)$$

The middle arc in the frequency range of ~10 Hz to ~10 kHz is attributed to the resistance and capacitance, R_2 and C_2, of the concrete microstructure and its composition at the steel-concrete interface. John et al. [47] and Lemoine et al. [44] proposed that this arc is due to the calcium hydroxide (lime) precipitation on the steel surface during the hydration of cement paste. Other researchers have attributed this arc to the corrosion product layers having lime precipitation [49,49]. The carbonated concrete, where calcium hydroxide is consumed in the carbonation process, has a flattened curve at the same frequencies [35]. The third arc at around 100 kHz–1 MHz frequency, is due to the bulk concrete resistance, i.e., $R_1 = R_c$, and the capacitance, $C_1(Q_1) = C_c$. At a frequency range of 1 MHz–8 MHz, another resistance, R_0, is observed. No physical meaning is assigned to this resistance in the corrosion system inside RC. Several researchers have disregarded this resistance [35,44,46].

The EC at lower frequency of 0.001 Hz–0.1 Hz yields similar conclusions to other rebar in terms of the electrode characteristics R_{ct}, C_{dl}, and W. However, in the 10 Hz–300 KHz range, the behavior is different due to the epoxy coating characteristics, R_{Ep} and C_p. The values of R_{Ep} and C_p are different than that of rust layer characteristic, R_2, and C_2 on the uncoated rebar. The charge transfer resistance of EC is higher than those of MS, HC and HS, which indicates a passive state of steel underneath the epoxy coating.

Fig. 10 shows the fitting of Nyquist and Bode plots of an MS sample. Both circuits have good fitting with the experimental EIS spectra.

The average values of the impedance parameters obtained by fitting the model are provided in Table 6. The concrete resistance was observed to be between 28 kΩ.cm^2 and 47 kΩ.cm^2, while the capacitance of the bulk concrete was between 10^{-3} $\mu F \cdot cm^{-2}$ and 10^{-5} $\mu F \cdot cm^{-2}$. The resistance, R_2, of the rust products and the lime layer on the steel-concrete interface was 6 kΩ.cm^2, 15 kΩ.cm^2, and 13 kΩ.cm^2 for HS, MS, and HC steel, respectively. While for EC, the value of R_{Ep} was 80 kΩ.cm^2. The higher R_2, for HC steel and MS than HS samples, indicates that the middle arc observed in the Nyquist plot originated from the electrode surface, and related to corrosion products and calcium hydroxide formation on the steel surface. The capacitance of this second RC

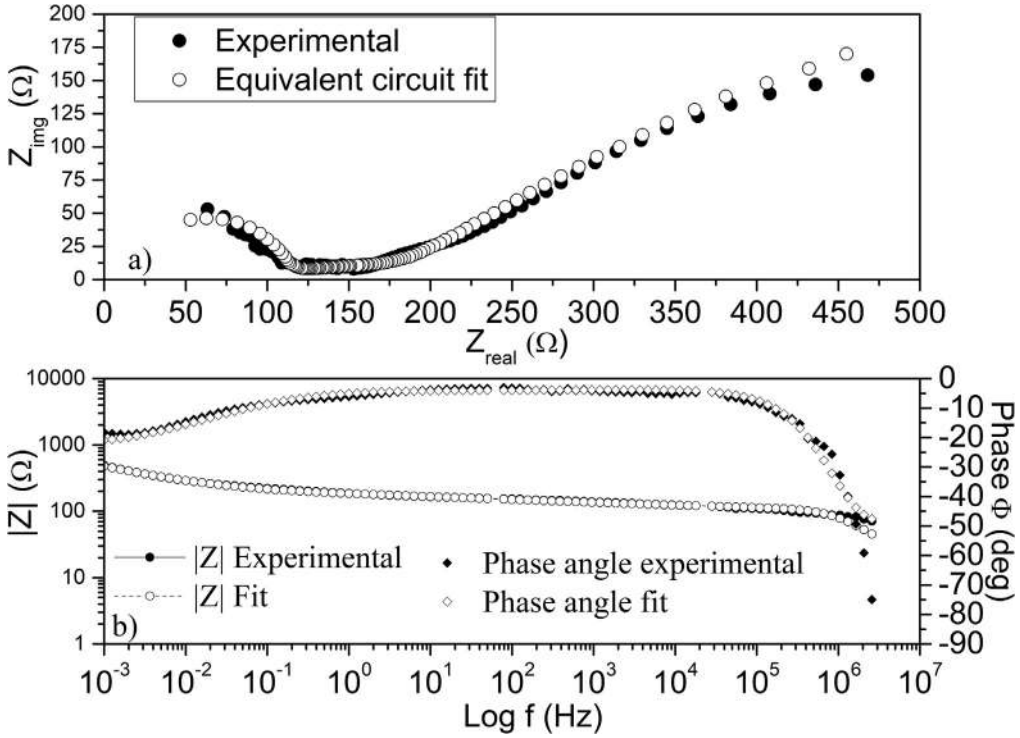

Fig. 10. Curve fitting of equivalent circuit model against the experimental data. a) Nyquist plot, b) Bode plot of a MS sample.

Table 6
Average values of electrochemical impedance parameters.

	Rc kΩ.cm^2	CPE ($\boldsymbol{Q}_1$) ohm^{-1} s^n	$\boldsymbol{n}_1$ –	Cc μF/cm^2	R_2 kΩ.cm^2	CPE ($\boldsymbol{Q}_2$) ohm^{-1} s^n	$\boldsymbol{n}_2$ –	C_2 μF/cm^2	R_{ct} kΩ.cm^2	CPE ($\boldsymbol{Q}_{dl}$) ohm^{-1} s^n	$\boldsymbol{n}_3$ –	C_{dl} F/cm^2	W Ω.cm^2.s$^{-1/2}$
MS	39	2.12E−04	0.70	9.58E−04	15	1.55E−04	0.65	4.07E−04	21	1.29E−02	0.38	6.00E−04	0.058
HC	47	5.24E−04	0.45	3.76E−03	13	3.50E−04	0.70	3.58E−03	34	3.13E−02	0.51	4.55E−05	0.013
HS	28	5.56E−05	0.83	1.97E−04	6	4.49E−03	0.63	1.03E−01	13	7.42E−02	0.33	1.68E−02	0.097
EC	30	5.06E−06	0.61	2.96E−05	80	3.72E−08	0.80	7.79E−06	136	1.60E−03	0.39	1.03E−05	0.039

element was $1.03 \times 10^{-1}\ \mu F \cdot cm^{-2}$, $4.07\ 10^{-4}\ \mu F \cdot cm^{-2}$ and $3.58 \times 10^{3}\ \mu F \cdot cm^{-2}$ for HS, MS and HC, respectively. The HS samples showed a higher capacitance in this frequency range than MS and HC. The EC showed the highest resistance for this arc; however, the lowest capacitance of $7.79 \times 10^{-6}\ \mu F \cdot cm^{-2}$ was also observed. This is attributed to the insulation properties of the epoxy coating. The values are normalized over the total embedded area, i.e., the whole length of rebar. Since the EIS technique apply alternating current (AC) impulse that can pass through the epoxy coating, it is concluded that whole length of the EC was polarized.

The R_{ct}, which is equivalent to R_p, was observed to be $136\ k\Omega \cdot cm^2$, $34\ k\Omega \cdot cm^2$, $21\ k\Omega \cdot cm^2$ and $13\ k\Omega \cdot cm^2$ for EC, HC steel, MS and HS, respectively. Although, R_p of EC was higher than those of the other steel rebar, these values suggest a minor corrosion current was going through EC. These currents were generate due to the corrosion of the electrical connections. The double layer capacitance was obtained as $600\ \mu F \cdot cm^{-2}$, $45\ \mu F \cdot cm^{-2}$, $1680\ \mu F \cdot cm^{-2}$ and $10\ \mu F \cdot cm^{-2}$ on MS, HC, HS and EC, respectively. The higher capacitance of the double layer in the case of HS and MS indicates the iron ion deposition on the steel surface and a higher corrosion activity. The Warburg impedance coefficient was found to be lower for HC than MS and HS. In the case of EC, the impedance to diffusion through epoxy as a medium is less, which suggests that species such as chloride and water might diffuse through coating over time.

Although the LPR and EIS techniques suggest that the R_p values were in close agreement (see Fig. 11), the EIS technique showed slightly lower R_p for uncoated rebar. The previous studies indicate that the EIS provide higher values than LPR. Pradhan and Bhattacharjee [50] have observed that EIS yields 9% higher R_p values

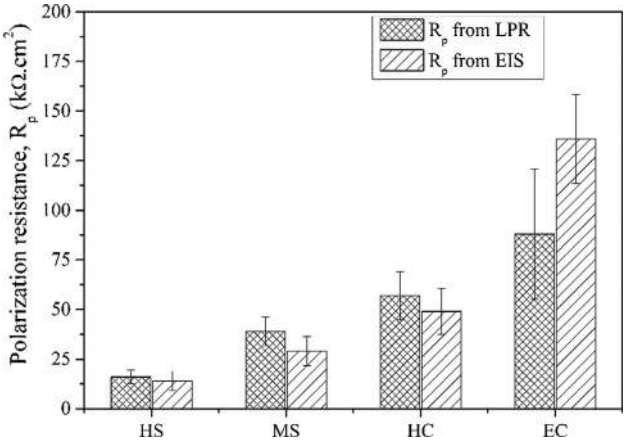

Fig. 11. Linear polarization resistance and charge transfer resistance calculated by LPR and EIS techniques.

than LPR. As the margins are very narrow, and the fact that R_p measurements are affected by humidity, temperature, and concrete quality, the results from both techniques are in the acceptable range in this study. In the case of EC, the R_p was also measured by LPR to validate the values obtained by the EIS technique. The results are shown in Fig. 11. The results in this study indicate that the EIS can be used to detect the corrosion of steel rebar underneath the epoxy coating and breakage or holidays in the epoxy.

4.6. Tafel polarization curves

Fig. 12 shows the Tafel polarization curves for all the samples of MS, HC and HS rebar. The scatter in the results is due to different OCP values. An interpretation of these curves was performed to obtain the corrosion parameters. The anodic branch shows the activation-controlled polarization indicated by the linear curve in the Tafel region up to +200 mV. While, the cathodic branch showed a sudden rise in the current values near −200 mV polarization, which suggests the mass diffusion of oxygen and hydrogen. This region was ignored while obtaining the Tafel slope constants, instead the slope of the linear portion was considered. Mohamed et al. [17] observed similar Tafel polarization behavior of MS and HC. Akhoondan and Sagüés [51] reported a modest concentration polarization at higher potential values of around ~200 mV while applying cyclic-polarization on conventional steel and 9% Cr rebar in concrete. They obtained corrosion parameters that were consistent with the literature and this study.

The statistical distributions of the measured I_{corr}, β_a, and β_c are presented using box plots in Figs. 13–15, respectively. The average I_{corr} values were found as 1.78 $\mu A \cdot cm^{-2}$, 0.661 $\mu A \cdot cm^{-2}$, and 0.316 $\mu A \cdot cm^{-2}$ for HS, MS, and HC, respectively. The average I_{corr} for EC was calculated using the EIS technique as 0.195 $\mu A \cdot cm^{-2}$, which is also presented in the same graphs for comparison purposes. The corrosion current densities according to Andrade et al. [52] were found to be in the range of "low" for EC, "moderate to high" for HC and "very high" for MS and HS. The corrosion current of the HC was found to be half of that of the MS in the active corrosion state. Similar ratio of corrosion currents between HC and MS has been reported by other researchers [17,53].

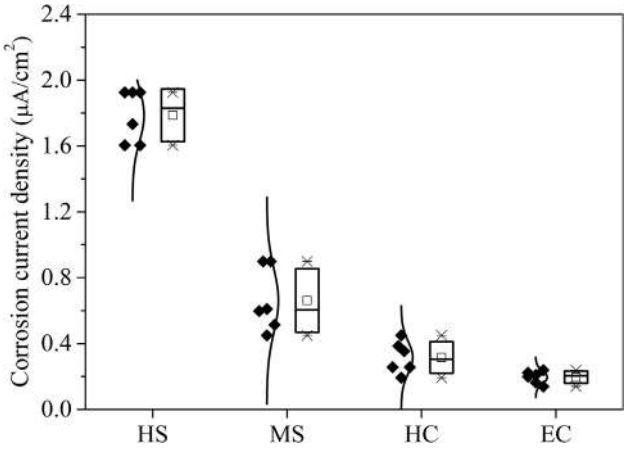

Fig. 13. Statistical distribution of corrosion current density of the studied steel rebar.

The average values of β_a were 416 mV/dec, 453 mV/dec and 497 mV/dec for MS, HC and HS, respectively. The average values of β_c were found as 152 mV/dec, 134 mV/dec and 162 mV/dec for MS, HC and HS, respectively. These Tafel slope constants are an indication of the reaction rate. The steeper the slope is, the higher is the rate of that half-cell reaction. β_c is normally two to three times lower than the β_a. This is due to the higher reduction rate of abundantly available oxygen at the steel-concrete interface.

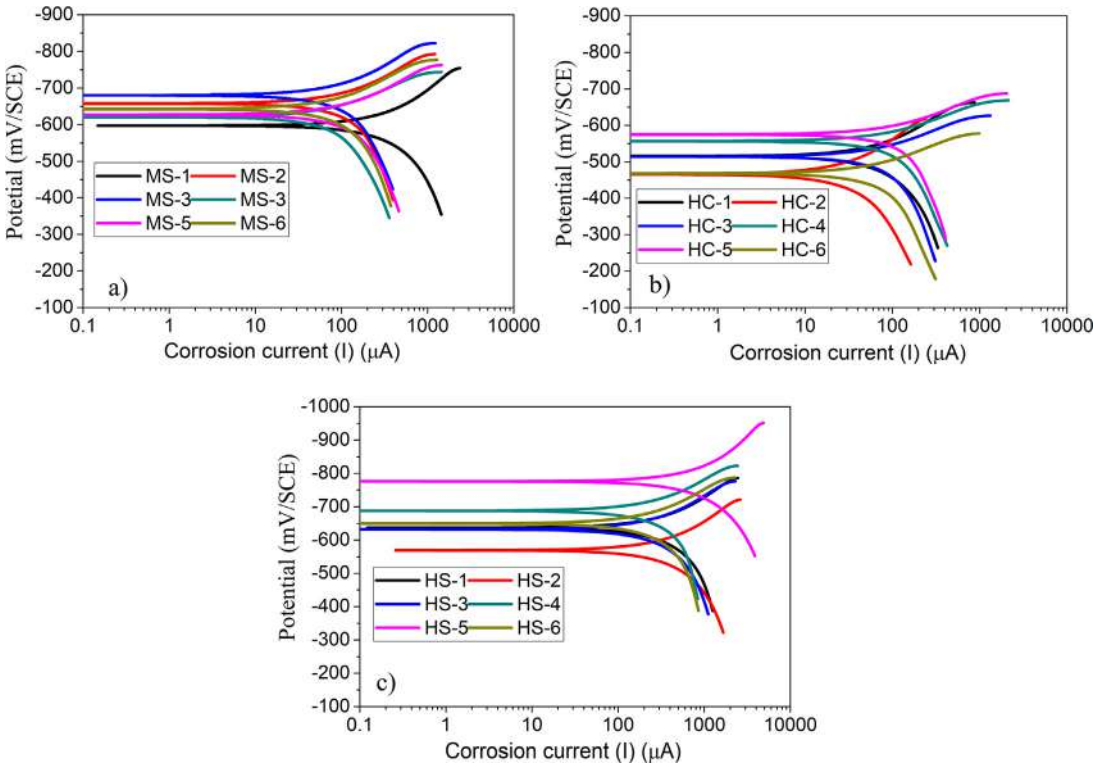

Fig. 12. Tafel polarization plots for a) MS, b) HC and c) HS.

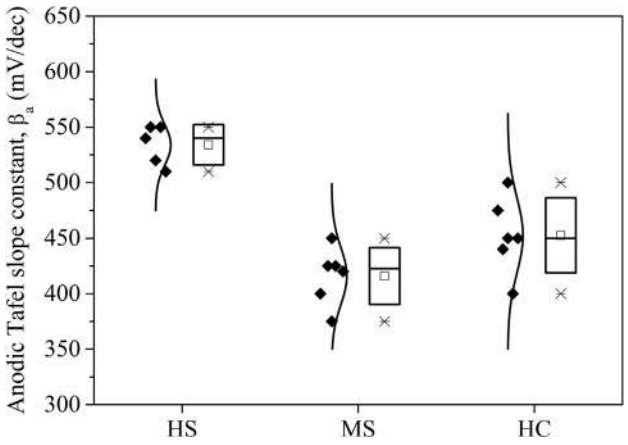

Fig. 14. Statistical distribution of anodic Tafel slope constants.

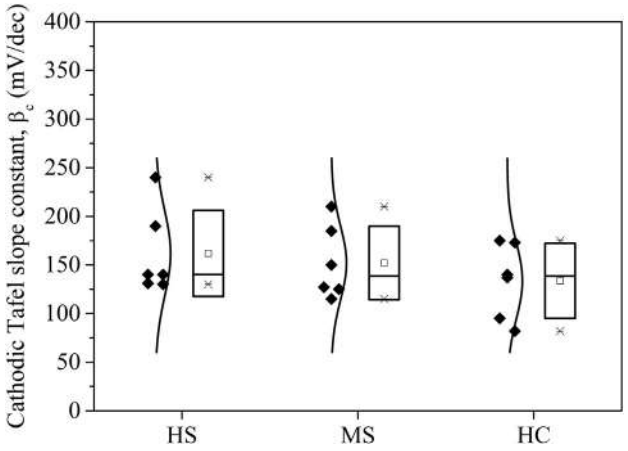

Fig. 15. Statistical distribution of cathodic Tafel slope constants.

During the iron oxidation in the anodic polarization (i.e., towards the positive potential), the electrons are forced out of steel and Fe^{2+} ions are freed at the steel-concrete interface. The already present oxide layers block these ions to move away from the steel surface and react with the hydroxyl; hence, building a positive charge barrier on the steel surface. It becomes difficult to extract the electrons out of the system; therefore, a reduced current and flattened anodic slope of the Tafel plot are observed.

Fig. 16 presents a comparison of the corrosion current densities on uncoated rebar calculated using the three electrochemical techniques. The measured currents from each technique were found to be in close agreement. In LPR and EIS techniques, to calculate i_{corr} using $i_{corr} = \frac{B}{R_p}$, the Stern and Geary constant B was recommended as 26 mV and 52 mV for active and passive steel, respectively, in [41]. In this study, the B was taken as 26 mV because all the steel rebar were in an active corrosion state. Using B equal to 26 mV yields i_{corr} values close to those obtained from the Tafel plots. However, the constant B depends on β_a and β_c $\left(B = \frac{\beta_a \beta_c}{\beta_a + \beta_c}\right)$, for its value to be equal to 26 mV, both β_a and β_c needs to be significantly lower than what has been observed in this study. With the values obtained, B would be in the range from 42 mV to 53 mV for active steel rebar. Other researchers [54–56] also reported higher values of anodic and cathodic Tafel slope constants (than 120 mV/dec). Hence, further research on Tafel parameters for steel rebar in concrete needs to be carried out in order to clearly understand the corrosion kinetics.

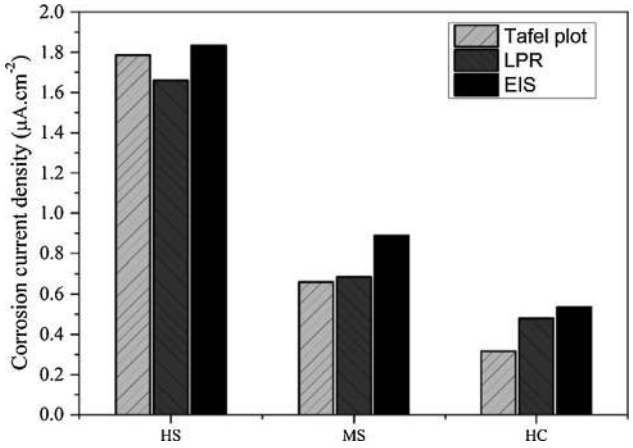

Fig. 16. Comparison of corrosion current densities from different techniques used.

4.7. Macrocell currents

Fig. 17 presents the macrocell currents for HS, MS and HC, until after a steady state condition was achieved. HC showed the minimum average macrocell current value of 67 μA, while MS and HS had average values of 127 μA and 327 μA, respectively. The macrocell corrosion current density (per unit area) was obtained as 0.42 μA/cm^2, 0.82 μA/cm^2 and 2.1 μA/cm^2 for HC, MS and HS, respectively. Compared to MS, the HC generated 48% less current. Cui and Krauss [16] observed 60% less macrocell corrosion in HC compared to MS in chloride contaminated concrete block samples with internally embedded cathode connected to corroding rebar through a 10 Ω resistor.

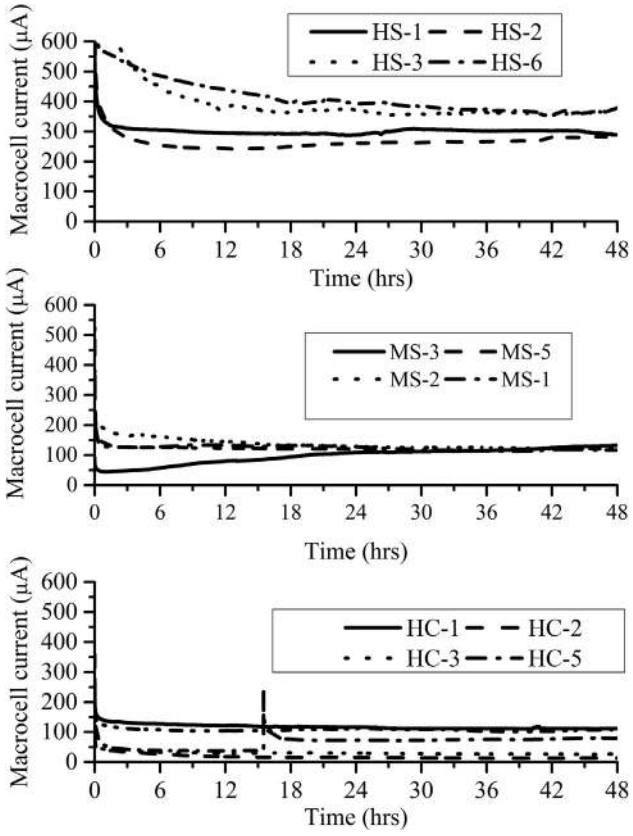

Fig. 17. Monitoring of macrocell current.

4.8. Visual inspection and corrosion rate

Fig. 18 shows the rebar from each type of steel after extraction from the concrete cylinders. The bars were cleaned chemically according to ASTM G1 [57] and then by mechanical brushing. The pits due to the chloride attack were visible on the steel surfaces. These pits were more frequent on MS and HS than on HC. The weight loss on one rebar from each type was measured with respect to the initial weight of the rebar. The total weight loss on HS, MS and HC was 3.05 g, 2.41 g, and 0.7 g, respectively. The peeled-off portion, and the patched edge of EC suffered corrosion as shown in Fig. 18d. Humidity and chloride penetrated into the patched epoxy and caused the corrosion (Fig. 18d). The rest of the EC bar was in a healthy state, based on a knife-peel test [58] with a rating of one, i.e., excellent state of epoxy with no breakage. The knife blade was not able to penetrate or chip off the epoxy.

The corrosion rate in mm/year was calculated using the corrosion current measurements according

$$Corrosion\,rate\,(\mathrm{mm/year}) = \frac{3272 I_{corr} E.W}{dA} \quad (3)$$

and weight loss measurements according

$$Corrosion\,rate\,(\mathrm{mm/year}) = \frac{KW}{ATD} \quad (4)$$

where I_{corr} is the corrosion current in μA, $E.W$ is the equivalent weight of steel (55.87 g/mol), d/D is the density of reinforcing steel in g/cm^3, A is the steel surface area in cm^2, K is a constant having a value of 87,600 to obtain corrosion rate in mm/year, and T is the time of exposure in hours. The corrosion rates, I_{corr} (from Tafel plots), were 0.042 mm/year, 0.015 mm/year, 0.0073 mm/year and 0.0078 mm/year for HS, MS, HC and EC, respectively (see Fig. 19). The gravimetric corrosion rates were 0.038 mm/year, 0.029 mm/year and 0.0087 mm/year for HS, MS and HC, respectively. It was assumed that the corrosion was initiated after 8 months (approx. half the exposure period). Although, HS and HC showed similar corrosion rates from both methods, the discrepancy in the corrosion rates of MS is attributed to the rough estimation of the corrosion initiation time. Additionally, the pitting formation could result in an underestimation of the corrosion rates when measured through electrochemical techniques.

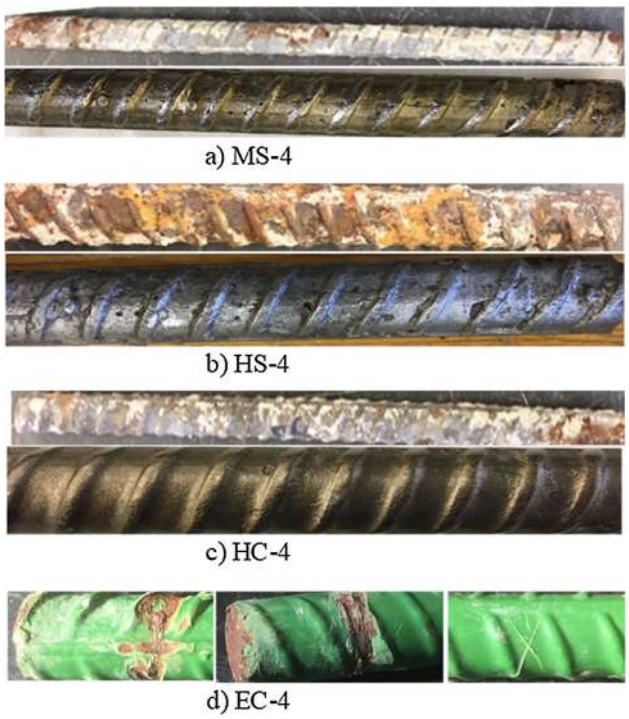

Fig. 18. Visual inspection of steel rebar after extraction from the concrete, and after cleaning according to ASTM G1 [57] and mechanical brushing. a) MS, b) HS, c) HC, and d) EC.

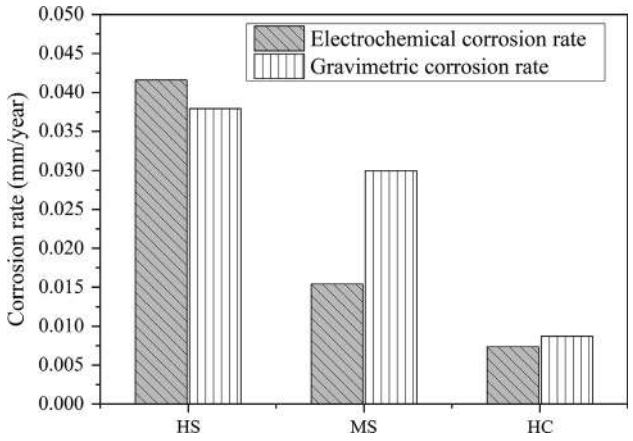

Fig. 19. Corrosion rate obtained from corrosion current density and gravimetric weight loss measurements.

5. A comparative discussion on steel rebar durability

Lower corrosion resistance of HS steel could be attributed to its alloy composition having 0.3% carbon (C) and 1.16% manganese (Mn). Mn is a more active metal than iron and forms oxide, which facilitates the metastable pitting on the steel surface. Park and Kwon [59] observed that with an increasing Mn content, the pitting potential shifts towards less electronegative values, and the passive film formed at the metal surface having Mn degrades easily. Since Mn is more active, it creates a macrocell within the matrix of metal and increases the corrosion rate on the steel surface [60]. In addition, the increase in the carbon content has also been linked to a decrease in the corrosion resistance of steel rebar [61].

In case of HC, the lower corrosion potential is due to the fact that few micro-galvanic cells form as a result of the microstructure and composition with Cr and Ni. The Cr reacts with oxygen and forms oxides, which protects the iron in the steel from corrosion. Corrosion resistance of HC during the polarization in LPR and Tafel plots at apparently active corrosion state is due to its microstructure, which is 100% packet martensite between untransformed sheets of austenite. In addition, since austenite is a more corrosion resistance phase; corrosion resistance of HC is higher. A more stable passive layer is formed on the steel surface containing chromium oxides. This passive film is less porous and requires a higher chloride threshold to break down [13,15,17].

The double layer capacitance in case of MS and HS is very high. Higher corrosion species containing iron ions could generate such higher capacitance. Flis et al. [62] observed that with an increase in anodic current (iron dissolution), the capacitance of the double layer increases. An increase in capacitance is also observed when there is dense packing of ions at the electrode surface. Vedalakshmi and Palaniswamy [42] observed this double layer capacitance on actively corroding rebar to be above 1000 $\mu F \cdot cm^{-2}$. The Warburg coefficient is lower due to the passive layer formed on the HC surface. Passive layer on HC contains lepidocrocite (FeOOH) and hematite (Fe_2O_3) [15], which are very dense and adhere well to the steel surface, hence, lowers the ion diffusion. This is why the Warburg impedance is higher in HC than MS, which has a magnetite (Fe_3O_4) as an oxide layer.

6. Summary and conclusions

The durability performance of four types of concrete rebar in terms of their corrosion resistance in harsh climatic conditions was evaluated. Southern Exposure test conditions were applied for 16 months by cyclically submerging the concrete cylinders containing steel rebar in 15% sodium chloride solution and drying in air. At the time of testing, the chloride ion concentration at the steel-concrete interface was 3–4 times higher than the normally considered threshold values for corrosion initiation of MS rebar.

The HCP suggested an active state of corrosion of the steel rebar after 16 months of exposure. At active corrosion state, the HCP of HC (−463 mV/SCE to −573 mV/SCE) always remained less electronegative than MS (−595 mV/SCE to −703 mV/SCE) and HS (−649 mV/SCE to −762 mV/SCE). The HS showed a more electronegative potential than the other uncoated steel rebar, which is attributed to the high carbon content. The EC had an HCP as high as −745 mV/SCE, which is believed to be due to the peeled portion of rebar at the electrical connections for testing.

The polarization resistance of steel rebar was obtained by LPR and EIS. The HC, even though in an active state of corrosion, offered 1.5–2 times more resistance to charge transfer than the MS. This means that the rate of corrosion of HC after initiation would be half of that of MS. The EIS technique was found to be a reliable method to assess the corrosion conditions of steel under the epoxy coating in the EC. The EIS showed that R_p for EC is higher than that of MS, HS and HC. There was no corrosion underneath the epoxy even in very high chloride concentrations. The polarization resistance suggested by EIS for EC was less than what was obtained from a passive state of rebar. This was due to the corrosion of the patched and electrical connection locations of the EC. The polarization resistance from LPR measured a similar range of values as indicated by EIS. This demonstrates that EIS could be used to determine the epoxy health and corrosion of the steel underneath the epoxy coating.

The average corrosion current densities from Tafel polarization curves were 1.78 $\mu A \cdot cm^{-2}$, 0.661 $\mu A \cdot cm^{-2}$ and 0.316 $\mu A \cdot cm^{-2}$ for HS, MS and HC, respectively. The corrosion current density of HC in the active state was half of that of MS and 1/6 that of HS. The EIS technique indicated that the corrosion current density in EC is 0.190 $\mu A \cdot cm^{-2}$, which is about 2.5 times lower than that of MS, and this corrosion current was only observed at the patched connections. Otherwise, the epoxy coating was in a healthy state under a heavy chloride attack.

The HCP drop from passive to active state was lowest for HC in comparison with the MS and HS during the macrocell formation. This produces less electromotive force to drive electrons from active to passive steel regions during the macrocell formation; and hence, less macrocell corrosion current is generated. This observation was verified by monitoring the macrocell corrosion current in HC, MS and HS. HC generated 48% less macrocell current than MS, given the same cathodic surface area was connected. In the case of EC, the macrocell cannot be formed until there are defects or holidays in the epoxy coating. The use of EC and HC is expected to enhance the life of RC structures, especially, the time-to-repair will be increased. Such corrosion resistant steel rebar are more suitable for regions where humidity and chloride concentration are higher, like the Middle East, where degradation of RC structures has become a major issue.

Declaration of Competing Interest

The authors declare that they have no known competing financial interests or personal relationships that could have appeared to influence the work reported in this paper.

Acknowledgments

The funding for this research was provided by the National Priorities Research Program of the Qatar National Research Fund (a member of the Qatar Foundation) under the award no. NPRP 7-410-2-169. The statements made herein are solely the responsibility of the authors and do not necessarily reflect the opinions of the Sponsor. Authors are also thankful to the Qatar Steel Company, Qatar Metals Coating Company, Mesaieed, Qatar, for providing the materials.

References

[1] G.H. Koch, M. Brongers, N.G. Thompson, Y.P. Virmani, J.H. Payer, Corrosion cost and prevent strategies in the United States, 2002. https://trid.trb.org/view.aspx?id=707382 (accessed 27.04.2017).
[2] R.C. Dunn, R.A. Ross, G.D. Davis, Corrosion monitoring of steel reinforced concrete structures using embedded instrumentation, NACE Corros. Conf. Expo (2010) 1–10.
[3] H.L. Lim, Assessing level and effectiveness of corrosion education in the UAE, Int. J. Corros. 2012 (2012) 1–10, https://doi.org/10.1155/2012/785701.
[4] S. Keßler, U. Angst, M. Zintel, B. Elsener, C. Gehlen, Epoxy-coated reinforcement in concrete structures: results of a Swiss pilot project after 24 years of field exposure, Mater. Corros. 67 (2016) 631–638, https://doi.org/10.1002/maco.201608863.
[5] D. Darwin, J. Browning, M. O'Reilly, L. Xing, J. Ji, Critical chloride corrosion threshold of galvanized reinforcing bars, ACI Mater. J. 106 (2009) 176–183. https://kuscholarworks.ku.edu/handle/1808/23270 (accessed 08.09.2017).
[6] ASTM A1035/A1035M-16b, Standard Specification for Deformed and Plain, Low-Carbon, Chromium, Steel Bars for Concrete Reinforcement, ASTM Int., West Conshohocken, PA, 2016. https://www.astm.org/Standards/A1035.htm (accessed 11.06.2018).
[7] P.E. Team, Purdue e-Pubs MMFX Microcomposite Steel (MMFX2), 2007. doi:10.5703/1288284315798.
[8] W. Pyc, Field Performance of Epoxy-Coated Reinforcing Steel in Virginia Bridge Decks, Virginia Tech, 1998. https://vtechworks.lib.vt.edu/handle/10919/29399 (accessed 02.04.2018).
[9] K.Z. Khaled, E. Vaca-Cortés, J.O. Jirsa, H.G. Wheat, R.L. Carrasquillo, Corrosion Performanc eof Epoxy-coated Reinforcement-BeamTests, Texas, USA, 1998.
[10] EN 206-1, EN 206-1, Institution, British Standards, London, 2000. https://shop.bsigroup.com/ProductDetail/?pid=000000000030148156 (accessed 07.04.2018).
[11] Ş. Erdoğdu, T. Bremner, I. Kondratova, Accelerated testing of plain and epoxy-coated reinforcement in simulated seawater and chloride solutions, Cem. Concr. Res. 31 (2001) 861–867, https://doi.org/10.1016/S0008-8846(01)00487-2.
[12] D.D.N. Singh, R. Ghosh, Unexpected deterioration of fusion-bonded epoxy-coated rebars embedded in chloride-contaminated concrete environments, Corrosion 61 (2005) 815–829, https://doi.org/10.5006/1.3278216.
[13] A. Fahim, A.E. Dean, M.D.A. Thomas, E.G. Moffatt, Corrosion resistance of chromium-steel and stainless steel reinforcement in concrete, Mater. Corros. 70 (2019) 328–344, https://doi.org/10.1002/maco.201709942.
[14] D. Darwin, J. Browning, T. Van Nguyen, C.E.J. Locke, Mechanical and corrosion properties of a high-strength, high chromium reinforcing steel for concrete, 2002. https://kuscholarworks.ku.edu/handle/1808/20449 (accessed 04.08.2018).
[15] V. Nachiappan, E.H. Cho, Corrosion of high chromium and conventional steels embedded in concrete, J. Perform. Constr. Facil. 19 (2005) 56–61, https://doi.org/10.1061/(ASCE)0887-3828(2005) 19:1(56).
[16] Fushuang Cui, Paul Krauss, Comparative corrosion testing and analysis of MMFX 2 rebars for reinforced concrete applications, 2008. http://mmfx.com/doc2/Comparative_Corrosion_Testing_Cui_Krauss.pdf (accessed 24.03.2017).
[17] N. Mohamed, M. Boulfiza, R. Evitts, Corrosion of carbon steel and corrosion-resistant rebars in concrete structures under chloride ion attack, J. Mater. Eng. Perform. 22 (2013) 787–795, https://doi.org/10.1007/s11665-012-0314-0.
[18] T. El Maaddawy, K. Soudki, A model for prediction of time from corrosion initiation to corrosion cracking, Cem. Concr. Compos. 29 (2007) 168–175, https://doi.org/10.1016/J.CEMCONCOMP.2006.11.004.
[19] U.M. Angst, Predicting the time to corrosion initiation in reinforced concrete structures exposed to chlorides, Cem. Concr. Res. 115 (2019) 559–567, https://doi.org/10.1016/J.CEMCONRES.2018.08.007.
[20] A. Jamali, U. Angst, B. Adey, B. Elsener, Modeling of corrosion-induced concrete cover cracking: a critical analysis, Constr. Build. Mater. 42 (2013), https://doi.org/10.1016/j.conbuildmat.2013.01.019.
[21] S. Morinaga, Prediction of service lives of reinforced concrete buildings based on rate of corrosion of reinforcing steel, 1988.
[22] ASTM A615/A615M-16, Standard Specification for Deformed and Plain Carbon-Steel Bars for Concrete Reinforcement, ASTM Int., West Conshohocken, PA, 2016. https://www.astm.org/Standards/A615.htm (accessed 11.06.2018).

[23] ASTM A775/A775M-17, Standard Specification for Epoxy-Coated Prefabricated Steel Reinforcing Bars 1, ASTM Int. West Conshohocken, PA, 2017, pp. 1–19. doi:10.1520/A0934.
[24] ASTM C1611/C1611M-14, Standard Test Method for Slump Flow of Self-Consolidating Concrete, West Conshohocken, PA, 2014. doi:10.1520/C1611_C1611M-14.
[25] ASTM C39/C39M-15a, Standard Test Method for Compressive Strength of Cylindrical Concrete Specimens, West Conshohocken, PA, 2015. doi:10.1520/C0039.
[26] AASHTO TP 95, Standard Method of Test for Surface Resistivity Indication of Concrete's Ability to Resist Chloride Ion Penetration, American Association of State Highway and Transportation Officials, Washington, DC, 2011. http://standards.globalspec.com/std/9863485/aashto-tp-95 (accessed 22.12.2017).
[27] Ha-Won Song, Velu Saraswathy, Corrosion monitoring of reinforced concrete structures – a review, Int. J. Electrochem. Sci. 2 (2007) 1–27.
[28] ASTM C1585-13, ASTM C1585-13 Standard Test Method for Measurement of Rate of Absorption of Water by Hydraulic-Cement Concretes, 2013. doi:10.1520/C1585-13.
[29] BS 1881 : Part-124, British Standard Testing concrete Part 124. Methods for analysis of hardened concrete, 1998. http://www.c-s-h.ir/wp-content/uploads/2015/10/BS-1881-Part-124-88.pdf (accessed 19.03.2017).
[30] J.P. Broomfield, in: Corrosion of Steel in Concrete: Understanding, Investigation and Repair, second ed., Taylor & Francis, 2006, https://doi.org/10.4324/9780203414606.
[31] G.K. Glass, N.R. Buenfeld, The presentation of the chloride threshold level for corrosion of steel in concrete, Corros. Sci. 39 (1997) 1001–1013, https://doi.org/10.1016/S0010-938X(97)00009-7.
[32] ASTM C876-09, Standard Test Method for Half-Cell Potentials of Uncoated Reinforcing Steel in Concrete, ASTM 91 (2015) 1–6. doi:10.1520/C0876-09.2.
[33] P. Gu, P. Xie, J.J. Beaudoin, R. Brousseau, A.C. impedance spectroscopy (I): a new equivalent circuit model for hydrated portland cement paste, Cem. Concr. Res. 22 (1992) 833–840, https://doi.org/10.1016/0008-8846(92)90107-7.
[34] G. Song, Equivalent circuit model for AC electrochemical impedance spectroscopy of concrete, Cem. Concr. Res. 30 (2000) 1723–1730, https://doi.org/10.1016/S0008-8846(00)00400-2.
[35] D.V. Ribeiro, J.C.C. Abrantes, Application of electrochemical impedance spectroscopy (EIS) to monitor the corrosion of reinforced concrete: a new approach, Constr. Build. Mater. 111 (2016) 98–104, https://doi.org/10.1016/J.CONBUILDMAT.2016.02.047.
[36] G. Kear, F.C. Walsh, The characteristics of a true Tafel slope, 2005. http://eprints.soton.ac.uk/49025/ (accessed 20.02.2013).
[37] ASTM WK37880, New Test Method for Measuring the Surface Resistivity of Hardened Concrete Using the Wenner Four-Electrode Method, 2013. https://www.astm.org/WorkItems/WK37880.htm (accessed 13.08.2017).
[38] M.G. Sohail, R. Kahraman, N.G. Ozerkan, N.A. Alnuaimi, B. Gencturk, M. Dawood, A. Belarbi, Reinforced concrete degradation in the harsh climates of the arabian gulf: field study on 30-to-50-year-old structures, J. Perform. Constr. Facil. 32 (2018), https://doi.org/10.1061/(asce)cf.1943-5509.0001204. 04018059 (1–12).
[39] W.P. Dias, Reduction of concrete sorptivity with age through carbonation, Cem. Concr. Res. 30 (2000) 1255–1261, https://doi.org/10.1016/S0008-8846(00)00311-2.
[40] ASTM C876-09, Test Method for Corrosion Potentials of Uncoated Reinforcing Steel in Concrete, 2009. http://www.astm.org/Standards/C876.htm (accessed 21.02.2013).
[41] C. Andrade, C. Alonso, Test methods for on-site corrosion rate measurement of steel reinforcement in concrete by means of the polarization resistance method, Mater. Struct. 37 (2004) 623–643, https://doi.org/10.1007/BF02483292.
[42] R. Vedalakshmi, N. Palaniswamy, Analysis of the electrochemical phenomenon at the rebar–concrete interface using the electrochemical impedance spectroscopic technique, Mag. Concr. Res. 62 (2010) 177–189, https://doi.org/10.1680/macr.2010.62.3.177.
[43] W.J. McCarter, S. Garvin, N. Bouzid, Impedance measurements on cement paste, J. Mater. Sci. Lett. 7 (1988) 1056–1057, https://doi.org/10.1007/BF00720825.
[44] M. Keddam, H. Takenouti, X.R. Nóvoa, C. Andrade, C. Alonso, Impedance measurements on cement paste, Cem. Concr. Res. 27 (1997) 1191–1201, https://doi.org/10.1016/S0008-8846(97)00117-8.
[45] M. Ismail, M. Ohtsu, Corrosion rate of ordinary and high-performance concrete subjected to chloride attack by AC impedance spectroscopy, Constr. Build. Mater. 20 (2006) 458–469, https://doi.org/10.1016/j.conbuildmat.2005.01.062.
[46] L. Lemoine, F. Wenger, J. Galland, Study of the corrosion of concrete reinforcement by electrochemical impedance measurement, in: Corros. Rates Steel Concr., ASTM International, 100 Barr Harbor Drive, PO Box C700, West Conshohocken, PA 19428-2959, 1990, https://doi.org/10.1520/STP25019S. pp. 118-118-16.
[47] D.G. John, P.C. Searson, J.L. Dawson, Use of AC impedance technique in studies on steel in concrete in immersed conditions, Br. Corros. J. 16 (1981) 102–106, https://doi.org/10.1179/000705981798275002.
[48] P. Lay, P.F. Lawrence, N.J.M. Wilkins, D.E. Williams, An a.c. impedance study of steel in concrete, J. Appl. Electrochem. 15 (1985) 755–766, https://doi.org/10.1007/BF00620572.
[49] L. Dhouibi-Hachani, E. Triki, J. Grandet, A. Raharinaivo, Comparing the steel-concrete interface state and its electrochemical impedance, Cem. Concr. Res. 26 (1996) 253–266, https://doi.org/10.1016/0008-8846(95)00214-6.
[50] B. Pradhan, B. Bhattacharjee, Performance evaluation of rebar in chloride contaminated concrete by corrosion rate, Constr. Build. Mater. 23 (2009) 2346–2356, https://doi.org/10.1016/J.CONBUILDMAT.2008.11.003.
[51] M. Akhoondan, A.A. Sagüés, Comparative cathodic behavior of ~9% Cr and plain steel reinforcement in concrete, Corrosion (2012), https://doi.org/10.5006/0010-9312-68-4-4.
[52] C. Andrade, M. Cruz Alonso, J. Antonio Gonzalez, An Initial Effort to Use the Corrosion Rate Measurements for Estimating Rebar Durability, 1990. www.astm.org (accessed 01.08.2018).
[53] J. Ji, D. Darwin, J.P. Browning, Corrosion Resistance of Duplex Stainless Steels and Mmfx Microcomposite Steel for Reinforced Concrete Bridge Decks, 2005.
[54] E. Redaelli, L. Bertolini, W. Peelen, R. Polder, FEM-models for the propagation period of chloride induced reinforcement corrosion, Mater. Corros. 57 (2006) 628–635, https://doi.org/10.1002/maco.200603994.
[55] M.E. Mitzithra, Detection of corrosion of reinforced concrete on cooling towers of energy production sites, 2013. http://thesesups.ups-tlse.fr/2135/ (accessed 01.07.2014).
[56] M.G. Sohail, Corrosion of steel in concrete: development of an accelerated test by carbonation and galvanic coupling, 2013. http://thesesups.ups-tlse.fr/1938/ (accessed 02.07.2014).
[57] ASTM G-I-90, Practice for Preparing, Cleaning, and Evaluating Corrosion Test Specimens, 1999. http://www.astm.org/DATABASE.CART/HISTORICAL/G1-90R99E1.htm (accessed 21.02.2013).
[58] Ontario Ministry of Transportation, Ontario Provincial Standards for Roads and Public Works, Kingston, Ontario, Canada, 1993.
[59] K. Park, H. Kwon, Effects of Mn on the localized corrosion behavior of Fe–18Cr alloys, Electrochim. Acta. 55 (2010) 3421–3427, https://doi.org/10.1016/J.ELECTACTA.2010.01.006.
[60] A.K. Singh, N. Rani, S. Kundu, Optimized Cr concentration in reinforcement steel for high corrosion resistance in simulated pore solution by electrochemical and cyclic corrosion tests, ISIJ Int. (2016), https://doi.org/10.2355/isijinternational.isijint-2016-088.
[61] C.X.S. Feilong, Li Xiaogang, Effects of carbon content and microstructure on corrosion property of new developed steels in acidic salt solutions, Acta Metall. Sin. (Engl. Lett.) 27 (2014) 115–123.
[62] J. Flis, J.L. Dawson, J. Gill, G.C. Wood, Impedance and electrochemical noise measurements on iron and iron-carbon alloys in hot caustic soda, Corros. Sci. (1991), https://doi.org/10.1016/0010-938X(91)90031-J.
[63] BS 4449:2005, Steel for the Reinforcement of Concrete. Weldable Reinforcing Steel. Bar, Coil and Decoiled Product. Specification (2005).
[64] M.G. Sohail, M. Salih, N. Al Nuaimi, R. Kahraman, Corrosion performance of mild steel and epoxy coated rebar in concrete under simulated harsh environment, Int. J. Build. Patho. Adaptation 37 (5) (2019) 657–678, https://doi.org/10.1108/IJBPA-12-2018-0099.